Actin branching in the initiation and maintenance of lamellipodia

Marlene Vinzenz[1], Maria Nemethova[1], Florian Schur[1], Jan Mueller[1], Akihiro Narita[2], Edit Urban[1], Christoph Winkler[3], Christian Schmeiser[3,4], Stefan A. Koestler[5], Klemens Rottner[5], Guenter P. Resch[1], Yuichiro Maeda[2] and J. Victor Small[1,*]

[1]Institute of Molecular Biotechnology, Dr. Bohr-Gasse 3, 1030 Vienna, Austria
[2]Nagoya University, Graduate School of Sciences, The Structural Biology Research Center and Division of Biological Science, Nagoya 464-8601, Japan
[3]RICAM, Austrian Academy of Sciences Vienna, 4040 Linz, Austria
[4]Faculty of Mathematics, University of Vienna, 1090 Vienna, Austria
[5]Institute of Genetics, University of Bonn, 53105 Bonn, Germany
*Author for correspondence (vic.small@imba.oeaw.ac.at)

Accepted 20 February 2012
Journal of Cell Science 125, 2775–2785

doi: 10.1242/jcs.107623

Summary

Using correlated live-cell imaging and electron tomography we found that actin branch junctions in protruding and treadmilling lamellipodia are not concentrated at the front as previously supposed, but link actin filament subsets in which there is a continuum of distances from a junction to the filament plus ends, for up to at least 1 μm. When branch sites were observed closely spaced on the same filament their separation was commonly a multiple of the actin helical repeat of 36 nm. Image averaging of branch junctions in the tomograms yielded a model for the in vivo branch at 2.9 nm resolution, which was comparable with that derived for the in vitro actin–Arp2/3 complex. Lamellipodium initiation was monitored in an intracellular wound-healing model and was found to involve branching from the sides of actin filaments oriented parallel to the plasmalemma. Many filament plus ends, presumably capped, terminated behind the lamellipodium tip and localized on the dorsal and ventral surfaces of the actin network. These findings reveal how branching events initiate and maintain a network of actin filaments of variable length, and provide the first structural model of the branch junction in vivo. A possible role of filament capping in generating the lamellipodium leaflet is discussed and a mathematical model of protrusion is also presented.

Key words: Actin, arp2/3 complex, Cytoskeleton, Electron tomography, Lamellipodia

Introduction

Cell migration is initiated by the polarized protrusion of cytoplasm, in the form of lamellipodia, filopodia or blebs (Lämmermann and Sixt, 2009; Small et al., 2002). Lamellipodia are thin sheets of cytoplasm 0.1–0.3 μm thick (Abercrombie et al., 1971) constructed from networks of actin filaments (Small et al., 1978). Pushing is effected by actin polymerization through insertion of actin monomers between the filament plus ends and the membrane interface (Wang, 1985) activated by nucleation and elongation factors recruited to the lamellipodium tip (Campellone and Welch, 2010; Chesarone and Goode, 2009; Rottner and Stradal, 2011). This polymerization gives rise to a retrograde flow of the actin network (Lai et al., 2008; Wang, 1985; Waterman-Storer et al., 1998) that is transduced into different rates of net protrusion depending on the degree of linkage of the lamellipodium with the substrate (Mitchison and Kirschner, 1988) and the proximal cytoskeleton (Alexandrova et al., 2008). In addition to protrusion, lamellipodia undergo phases of pause and retraction (Abercrombie et al., 1970), associated with reorientations of actin filaments (Koestler et al., 2008). Lamellipodia filaments can also be recruited into bundles to form filopodia (Höglund et al., 1980; Small, 1981; Svitkina et al., 2003). These reorganizations reflect a high degree of adaptation in lamellipodia architecture, in response to intrinsic and extrinsic signaling cues.

From two-dimensional electron micrographs of lamellipodia of fish keratocytes, cells that protrude continuously, it was proposed that the anterior zone of lamellipodia is composed of highly branched arrays of short filaments, 30–150 nm long (Svitkina et al., 1997; Svitkina and Borisy, 1999). The simultaneous observation that the Arp2/3 complex catalyzed the branching of actin filaments in vitro (Amann and Pollard, 2001) and localized specifically to lamellipodia (Svitkina and Borisy, 1999; Welch et al., 1997) formed the basis of the dendritic nucleation model of lamellipodia protrusion, which presumes that actin filaments must be short and stiff to push (Pollard and Borisy, 2003). Because actin filaments in lamellipodia are densely packed, the resolution of their spatial organization requires electron tomography, and in the first study using this approach (Urban et al., 2010) a dendritic array of short filaments was not found in lamellipodia of various cell types. Instead, the images revealed only few putative branch sites at the front of lamellipodia and an abundance of long filaments extending to the lamellipodium tip (Urban et al., 2010). One explanation of

Journal of Cell Science

these observations was that the branch frequency might be much lower than implied in the original model (Pollard and Borisy, 2003; Svitkina and Borisy, 1999), because only one branch is required per filament (Insall, 2011). To resolve this issue we generated a new series of tomograms of Rac-induced lamellipodia in which it was possible to track entire filament trajectories, from the plus to the minus ends, yielding the first complete structural model of actin filament organization. Our findings confirm that actin branches are not concentrated at the lamellipodium tip but are distributed throughout the lamellipodium and link actin filaments of variable length into subsets that together make up the filament network. We also present a model of the actin branch junction in vivo at 2.9 nm resolution and show that actin side branching and end branching are, respectively, involved in the initiation and maintenance of lamellipodia. Our findings also suggest a hitherto unexpected role of filament capping in molding the lamellipodium leaflet.

Results

Actin branching and network organization in protruding and treadmilling lamellipodia induced by Rac

To achieve a reproducible state of lamellipodia activity we used mouse NIH3T3 cells that were transfected with constitutively active L61Rac. Transfected cells typically exhibited an unpolarized shape with wide lamellipodia around most of their periphery. We injected these cells with L61Rac to also ensure a consistent Rac response, monitored by live cell imaging, and fixed and processed the same cells for electron tomography after negative staining (negative stain ET). Fig. 1A–F shows an example of correlated live-cell imaging and electron tomography of a cell in which a lamellipodium, extending beneath a retracting ruffle, protruded continuously at 2 μm/minute up to the point of fixation (Fig. 1D,E, black arrows; supplementary material Movie 1). A section of the tomogram (Fig. 1F) shows the actin filaments, readily identified from their characteristic helical substructure, organized in a diagonal array. The thickness of Rac-induced lamellipodia was generally less than that observed in fibroblasts used in our previous study (Urban et al., 2010) and resulted in a corresponding improvement in resolution. Actin filaments were tracked through the tomograms using both manual and automatic protocols (Materials and Methods; supplementary material Fig. S1; the original tomograms and accompanying data are available from the corresponding author.). Superposition of the three-dimensional maps of filament trajectories obtained by these two methods (supplementary material Fig. S1) showed a close correlation, whereby any differences served to indicate where filaments were either missed or mistaken for background material. Fig. 1G shows the filament trajectories obtained from complementation of manual and automatic tracking in the projection of the tomogram corresponding to the region in Fig. 1F. Branch junctions (Fig. 1G, red dots) were identified manually from characteristic end-to-side associations of filaments in an angular range of 60–90° in the same z-level, accompanied by additional material at their apex (Fig. 1F, black circles; Fig. 7). Tracking of filaments through the entire tomogram, extending 1 μm behind the lamellipodium tip, revealed filament subsets linked in this tomogram by three to seven branch junctions, examples of which are highlighted in Fig. 2A and supplementary material Movie 2. Individual filaments were also identified that extended beyond the tomogram and some showed no association with branch points; examples are indicated in black in Fig. 2A. The plus ends of filaments are marked with black dots. Computation of the orientation of filament segments in the manually and automatically tracked models showed a broad angular distribution approximating a diagonal network (supplementary material Fig. S1E,F). The total actin filament length in the tomogram computed from manual tracking was 154 μm and by automatic tracking 180 μm, the difference being mainly due to filaments at the periphery of the tomogram excluded during manual tracking. Taking the automatic tracking figure and the total number of branch junctions of 224 we obtained an average of 1 branch per 0.8 μm of traversed filament length. In a tomogram taken from a region in the same cell that was undergoing treadmilling at 2.3 μm/minute at the time of fixation (Fig. 1D,E, white arrowhead; supplementary material Movie 1) we tracked filaments manually through the entire tomogram (supplementary material Fig. S2). From a total of 351 filaments, 87 were unbranched (within the tomogram) and the remaining 264 filaments were divided into 88 subsets (supplementary material Fig. S2) linked by a total of 226 branch junctions, with up to 10 branch junctions within one subset. The total filament length within the tomogram was 171 μm, corresponding to an average frequency of one branch per 0.75 μm of traversed filament length.

Another example of a lamellipodium in a Rac-transfected and microinjected NIH3T3 cell fixed during treadmilling, with no net protrusion is shown in Fig. 3 and supplementary material Movie 3. The treadmilling rate in the region of the tomogram (indicated by an arrow in Fig. 3B–C), measured from the fluorescent actin label was 1.8 μm/minute. The tomogram of the treadmilling zone (Fig. 3E–G) revealed a filament organization, orientation and branch density similar to the protruding and treadmilling lamellipodia in Fig. 1 and supplementary material Fig. S2. Three branch junctions in the plane of the tomogram section (Fig. 3E) are encircled in black and the projected positions of all branch junctions within the tomogram are marked in red in Fig. 3F,G, showing a uniform spread of branch distribution in this anterior region. Filament trajectories and examples of filament subsets and branch junctions are shown in Fig. 3G and supplementary material Movie 4. The phenotypes of lamellipodia described are not the only ones observed in L61Rac-transfected cells. In cells exhibiting regular ruffling activity in the treadmilling regions we observed a substantial proportion of filaments oriented more parallel to the cell front, indicating considerable modification according to different modes of motile activity (Koestler et al., 2008). Here we focus on wide lamellipodia undergoing constant treadmilling or protrusion.

Because fish keratocytes have been used as a model of persistent lamellipodia protrusion (Svitkina et al., 1997; Urban et al., 2010) we re-examined these cells by electron tomography. In negatively stained preparations of lamellipodia thin enough to allow tracking of filaments for several hundred nanometers behind the lamellipodium tip (supplementary material Fig. S3A,B) we found that branch junctions were not concentrated at the front, but were distributed more or less uniformly over the anterior 750 nm (supplementary material Fig. S3B,D). Typical junction sites are shown in supplementary material Fig. S3C. Similar to the mouse NIH3T3 cells, we observed filament subsets linked by branch junctions with a wide variation in separation between the branch junction and the filament plus end (supplementary material Fig. S3B).

Initiation of lamellipodia involves side branching

In experiments on sea urchin coelomocytes Henson et al. showed that single cells could repair wounds in the cytoplasm inflicted by

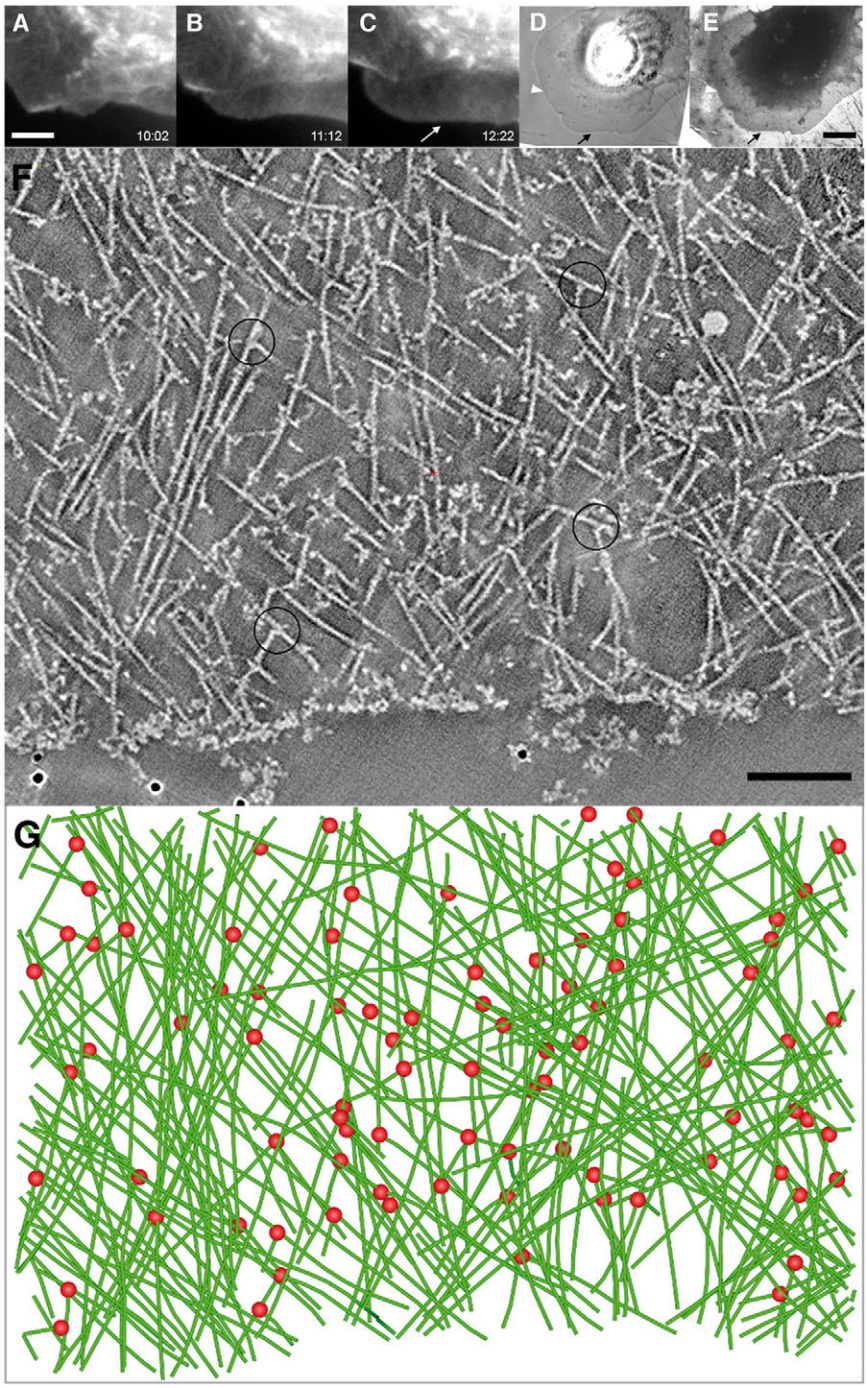

Fig. 1. Actin branches in a protruding lamellipodium. (**A–C**). Movie frames of the edge of an NIH3T3 cell that was co-transfected with Lifeact–GFP and constitutively active Rac. Prior to taking the movie sequence the cell was also injected with constitutively active Rac to consolidate the response (supplementary material Movie 1). (**D**) Phase-contrast image of the cell in A-C that was fixed immediately after the stage shown C, at the end of the protrusion phase (at a position indicated by the white arrow in C and the black arrow in D). (**E**) Electron micrograph of the fixed and negatively stained cell. The region indicated by white arrowheads in D and E is the treadmilling region (see text, supplementary material Movie 1, Fig. S2). (**F**) 7.5 nm section of electron tomogram taken from the region indicated by arrows in C–E. Black circles highlight four branch junctions. (**G**) Projection of a three-dimensional (3D) model of the actin network corresponding to the region shown in F and obtained by combining results of manual and automatic tracking of filaments through the tomogram. Green lines, actin filaments; red dots, branch junctions. Scale bars: A, 5 μm; E, 10 μm; F, 100 nm.

a microneedle and that wound closure involved the induction of lamellipodia-like structures, containing both actin and Arp2/3 complex components (Henson et al., 2002). We have adapted the same assay to vertebrate cells and have exploited this model system to capture the initial stages of lamellipodium formation (supplementary material Movie 5). An example of wound induction and closure is shown for a B16 melanoma cell in Fig. 4A. Fluorescence microscopy with different probes showed that typical lamellipodia components, in addition to actin, were recruited to the wound site, including VASP, ArpC5, Abi (Fig. 4B–D) and WAVE2 (not shown). Myosin II was not recruited in detectable amounts to the wound edge (Fig. 4D) and experiments with the myosin light chain kinase inhibitor (ML-7) showed that myosin contractile activity was not essential for wound closure (data not shown), as also noted for wounds induced in coelomocytes (Henson et al., 2002).

Using correlated live cell imaging and electron tomography we investigated different stages in the formation of lamellipodia during intracellular wound repair in B16 melanoma cells, NIH3T3 fibroblasts and fish keratocytes. A tomogram section of a hole in a relatively late stage of repair in a B16 melanoma cell is shown in Fig. 4E. The original periphery of the hole is delineated by a parallel bundle of actin filaments (Fig. 4E, black arrow), presumably derived from filaments that pre-existed in the

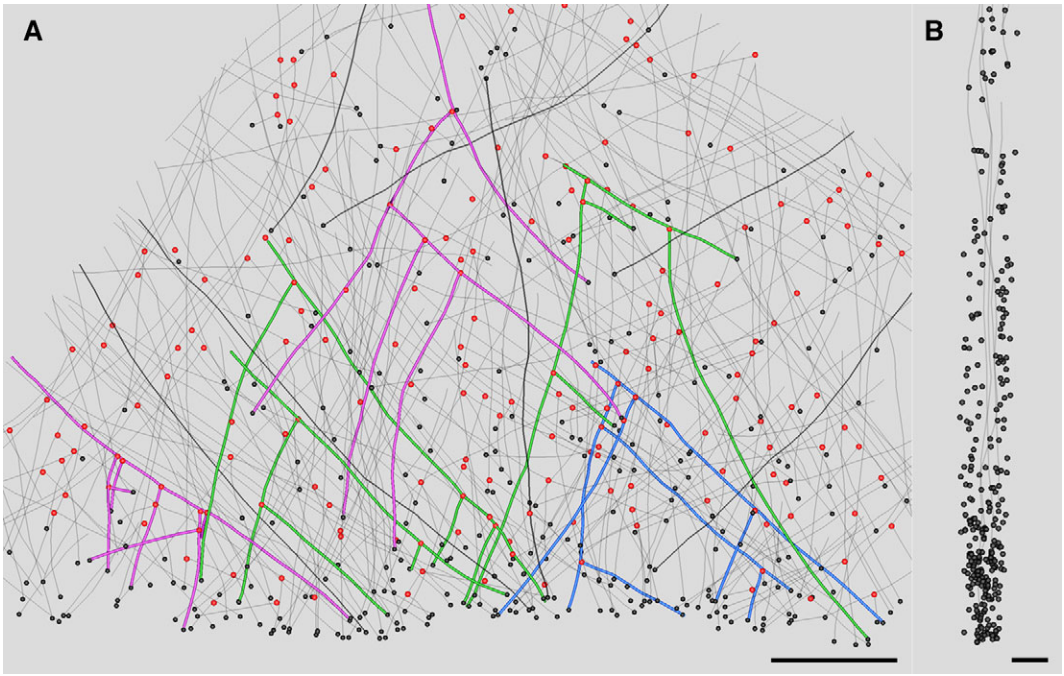

Fig. 2. Actin branches link filament subsets. (**A**) 2D projection of 3D model of filament trajectories (lines) in the entire tomogram of the lamellipodium shown in Fig. 1. Thicker colored lines highlight examples of filament subsets linked by branch junctions (red dots). Black dots indicate plus ends of filaments. Thickened black lines indicate examples of filaments lacking associated branch junctions within the volume of the tomogram. (**B**) Side view of the anterior part of the model including a filament subset (grey) and the filament ends (black dots) to illustrate distribution of trailing plus ends close to the surfaces of the network. Scale bars: A, 200 nm; B, 25 nm.

lamella cytoskeleton (Fig. 4F). Otherwise, the network shows the characteristic distribution of branch junctions and filament subsets observed in typical lamellipodia (highlighted in blue in Fig. 4E). The earliest stages of lamellipodium formation were captured by fixing cells as soon as possible after wounding, in practice within the first 5 seconds after application of the micropipette to the cell surface. Examples of the initiation of wound repair in a NIH3T3 cell (Fig. 5A,B) and a keratocyte (Fig. 5C,D) show that the first actin branches occurred from the sides of filaments parallel to the periphery of the hole. In some cases many branches emerged from the same filament (Fig. 5A,D), spaced 36 nm apart.

Characterization of branch junctions and extensions to filament plus ends

Quantitative analysis of tomograms of Rac-induced lamellipodia is shown in Fig. 6. Measurements of the distance from a branch junction to the filament plus end revealed a wide distribution: up to 800 nm (Fig. 6A), close to the maximum trajectory measureable within a single tomogram. Over the anterior 1 μm or so of the lamellipodium network the branch density declined gradually, in parallel with actin filament density (Fig. 6C). This decline continued across the breadth of the lamellipodium, as revealed by the gradient of mCherry–actin and GFP–ArpC5 labeling in living cells (supplementary material Fig. S4). Given sufficient resolution of the actin helix in electron micrographs, it is possible from the tilt of the subunits to determine actin filament polarity (Narita and Maéda, 2007; Steinmetz et al., 1997). Cross correlation analysis of actin filaments in tomograms of negatively stained lamellipodia confirmed that the filament plus ends were directed forwards (see Materials and Methods). Filament tracking in tomograms of negatively stained cytoskeletons showed that filament plus ends were not localized exclusively to the lamellipodium tip, but distributed over the first 1 μm of the lamellipodium network at a density (behind the tip) comparable to that of branch junctions (Fig. 6D). Notably, the plus ends located behind the lamellipodium tip were restricted almost exclusively to the surface of the actin network (Fig. 2B), as also noted previously (Urban et al., 2010). Because the negatively stained samples showed some collapse in the z-direction we performed cryo-electron tomography (cryo-ET) on cytoskeletons of NIH3T3 cells transfected with constitutively active L61Rac to obtain complementary information about the spatial localization of filament ends. By imaging regions of cytoskeletons in vitreous ice over holes in the support film we obtained good filament resolution (supplementary material Fig. S5A). Owing to the need for low dose imaging and tilting around only one axis with the cryo-ET samples the actin helix was not resolved, but branch junctions could be identified (supplementary material Fig. S5, Movie 6; Fig. 7C) and filaments could be tracked to their anteriorly directed plus ends. As shown in the cross section of the tomogram model in supplementary material Fig. S5D, filament plus ends were located more or less exclusively at the surface of the lamellipodium network, either at the extreme tip or on the dorsal or ventral surface.

Rouiller et al. used cryo-EM and negative stain EM to derive a model of the actin–Arp2/3 complex in vitro (Rouiller et al., 2008). A selected gallery of branch junctions in lamellipodia of negatively stained NIH3T3 cell cytoskeletons is shown in Fig. 7A,B. By image averaging 654 branches of this type we obtained a 2.9 nm model of the in vivo branch junction (Fig. 7D), which was very similar to that obtained for the in vitro complex

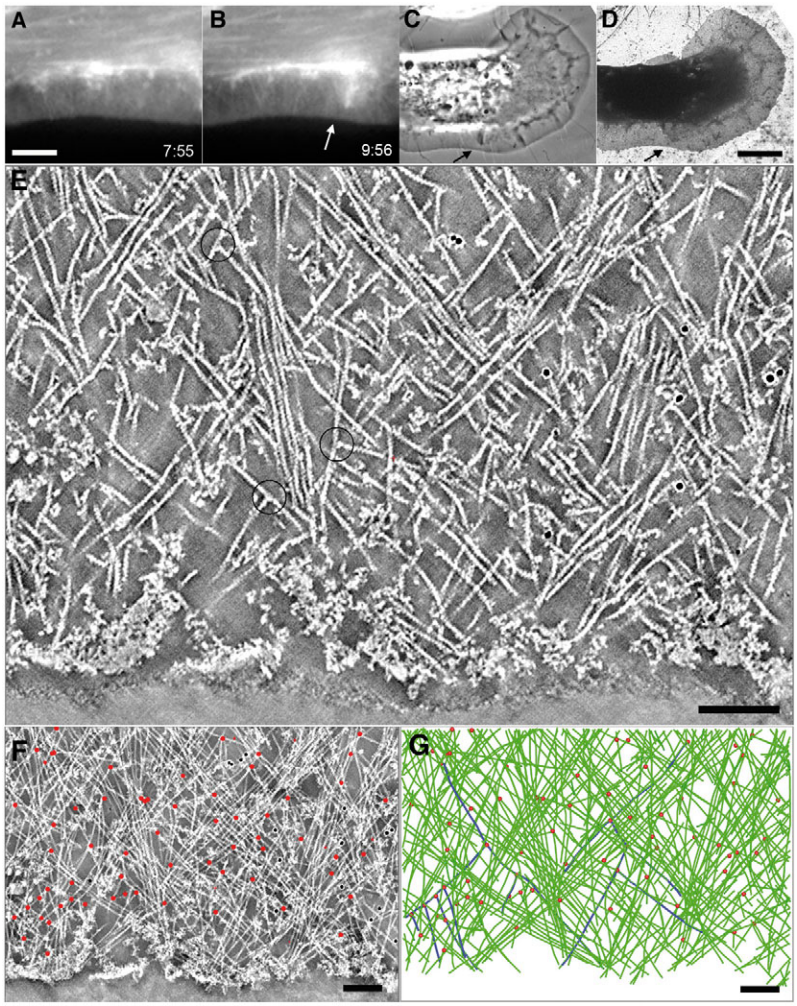

Fig. 3. Automatic filament tracking and actin branches in a treadmilling lamellipodium. (**A**,**B**) Movie frames of the edge of a treadmilling NIH3T3 cell that was co-transfected with Lifeact–GFP and constitutively active Rac. Prior to taking the movie sequence the cell was also injected with constitutively active Rac to consolidate the response. (**C**) Phase-contrast image of the cell in B immediately after fixing. (**D**) Electron micrograph of the fixed and negatively stained cell. The treadmilling rate before fixation was 1.9 µm/minute. (**E**) Section of an electron tomogram taken from the region indicated by arrows in B and C. Black circles indicate three branch junctions in the tomogram section. (**F**) Stack of 25 tomogram sections to show general organization of the actin network, with the positions of branch junctions superimposed (red dots). (**G**) 3D model obtained by automatic and manual tracking of actin filaments (green) through the tomogram in E and F, showing branch junctions (red dots) and two filament subsets linked by branch junctions (blue). Scale bars: A, 5 µm; D, 10 µm; E, 100 nm; F,G, 100 nm.

(Rouiller et al., 2008). The similarity was confirmed by fitting the crystal structure of the Arp2/3 complex in the extra material at the branch point (Materials and Methods; Fig. 7D; supplementary material Movie 7). The average branch angles measured in different cell types, in both negatively stained and frozen cytoskeletons are presented in Fig. 7E. From a total of 600 branches in six tomograms of negatively stained NIH3T3 cell cytoskeletons the branch angle was 73±8°, compared with 77±8° (n=90) in the cryo samples. For B16 melanoma cells and fish keratocytes the branch angles were respectively 73±9° (n=120) and 74±8° (n=264). Although the frequency of branches on actin filaments was in the order of one branch per 0.8 µm of filament length, closely spaced branches lying in the same plane were frequently seen and were notably separated by multiples of the actin helical repeat of 36 nm (36.7±4.7 nm, n=70; 71.2±4.6 nm, n=39; Fig. 6B). Occasionally, even more closely spaced branches were observed (Fig. 2, Fig. 6B), in which case the daughter filaments lay in different planes, as would be expected from the turn of the actin helix.

Discussion

The present study settles current differences about the organization of actin filaments in lamellipodia (Small et al., 2011; Yang and Svitkina, 2011) and provides the structural basis for advancing our understanding of the protrusion process. The improved resolution in our tomograms has facilitated the mapping of entire filament trajectories in three dimensions and the identification of actin branch junctions directly from their characteristic bifurcation angle and morphology. The similarity of the in vivo branch junction with the complex of actin and Arp2/3 in vitro (Rouiller et al., 2008) was striking and suggests that most of the material at the branch point arises from the Arp2/3 complex. Current efforts are directed towards obtaining a higher resolution structure of the in vivo branch to ascertain whether additional components are present.

In the current dendritic nucleation model it is proposed that actin filaments must be short and stiff to push (Pollard and Borisy, 2003). This idea stems from the observation of a ‘brush zone’ at the front of keratocyte lamellipodia, in which the actin filaments appeared highly branched (Svitkina and Borisy, 1999). At steady state it was presumed that most filaments were capped soon after nucleation and only a few of them continued to elongate and branch (Svitkina and Borisy, 1999). In a previous report we showed by electron tomography that the anterior region of keratocyte lamellipodia was not dominated by short filaments (Urban et al., 2010), and we identified only a few branch junctions. At the same time we overlooked the existence, shown here, of branch junctions distributed throughout the network. The distribution of branch junctions throughout the network explains the overall impression of long filaments in earlier studies

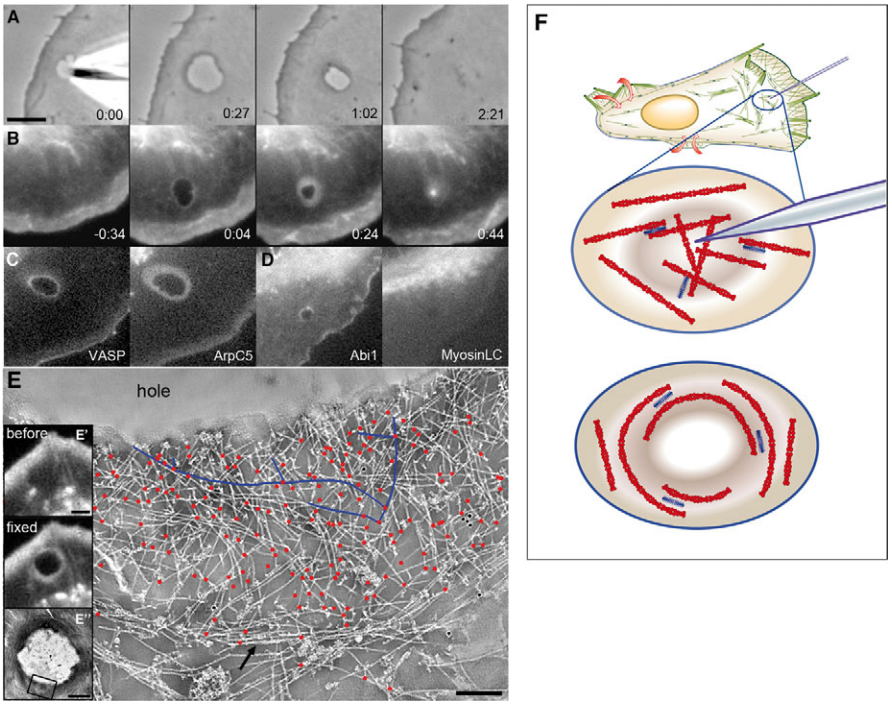

Fig. 4. Intracellular induction of lamellipodia. (**A**) Phase-contrast movie sequence showing lesion produced by a microneedle in a B16 melanoma cell and the subsequent repair of the induced hole. (**B**) Movie sequence of hole repair in a Lifeact–GFP-transfected B16 melanoma cell. (**C**,**D**) Movie frames of hole repair in B16 melanoma cells transfected with mCherry–actin (Nemethova et al., 2008), EGFP–Arp-p16 [ArpC5 (Lai et al., 2008)], mCherry–VASP (Koestler et al., 2008), GFP–Abi-1 (Lai et al., 2008) and mCherry–myosin-light-chain [re-cloned from an EGFP construct (Nemethova et al., 2008)]. (**E**) Correlated live-cell imaging (inset) and negative stain electron tomography of hole repair in a B16 melanoma cell. The main image shows a 15 nm section of the tomogram with projected positions of all branch junctions in the entire tomogram (red dots) and one filament subset (blue) superimposed. Arrow indicates an actin filament bundle marking the periphery of the hole immediately after induction. (**F**) Schematic illustration of hole induction, depicting recruitment of pre-existing filaments in the cytoplasm to the periphery of the hole, before lamellipodium formation. Blue lines indicate myosin filaments, which are dispensable for wound repair (see text). Scale bars: A–D, 5 μm; E, 250 nm; E′, 5 μm; E″, 1 μm.

of negatively stained lamellipodia by conventional electron microscopy (Höglund et al., 1980; Koestler et al., 2008; Small, 1981) as well as by electron tomography (Urban et al., 2010). As we now show, the actin filaments that make up the lamellipodium exhibit a continuum of lengths consistent with a steady nucleation of new filaments at the membrane through branching events and the retrograde flow of filament subsets linked by branch junctions. With this arrangement filaments of all lengths are engaged in pushing. The average frequency of approximately one branch per 0.8 μm of filament length suggests a molar ratio of bound Arp2/3 complex to actin of approximately 1:290 in Rac-induced lamellipodia (assuming 360 monomers of actin per micron of filament). Therefore, if the actin filaments need to be stiff to push, other cross-linkers such as filamin must be recruited to stabilize and stiffen the network (Flanagan et al., 2001). In this context, we propose the primary function of actin branching is to define network geometry.

In vitro studies of actin branching by the Arp2/3 complex suggested that actin ‘mother filaments’ were needed to catalyze the branching process (Machesky and Insall, 1998; Pollard and Borisy, 2003) preferentially from the sides (Amann and Pollard, 2001) or the ends of the mother filaments (Pantaloni et al., 2000). However, the origin of mother filaments in vivo remained a mystery (Pollard and Cooper, 2009). By monitoring the initial steps of lamellipodium formation we provide evidence for the origin of the mother filaments in vivo. The region behind the lamellipodium of motile cells contains actin filaments in various arrangements, either as single filaments or in bundles of various dimensions. In Rac-transfected fibroblasts and melanoma cells these regions contain mainly loose actin arrays (data not shown).

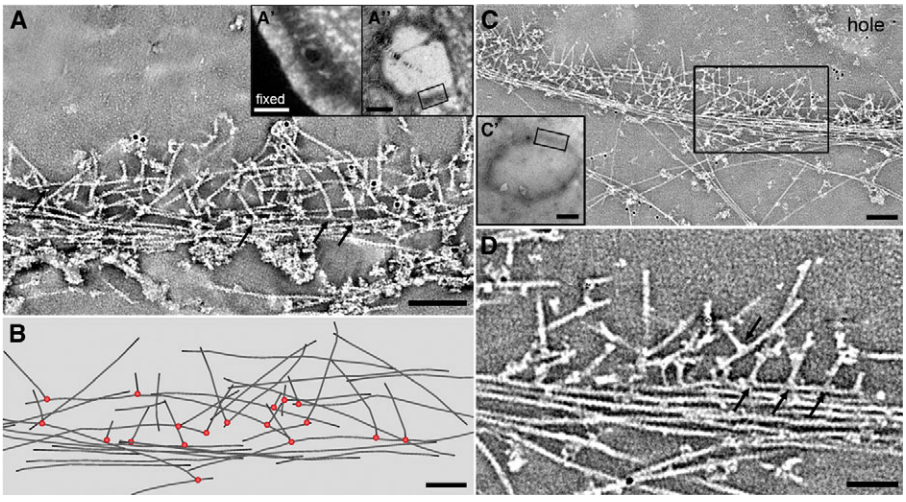

Fig. 5. Initiation of lamellipodia by side branching. (**A**) Negative stain electron tomogram section of the edge of a hole in an NIH3T3 fibroblast expressing Lifeact–GFP, fixed a few seconds after hole induction. Arrows indicate side branches from filaments parallel to the edge of the hole. Insets (**A′**,**A″**) show fluorescence microscopy and EM views of the hole. (**B**) Projection of 3D model of the actin network in A, showing actin filaments in grey and branch junctions as red dots. (**C**) Negative stain electron tomogram section of the edge of a hole in a fish keratocyte (as indicated by the boxed region in C′) fixed a few seconds after induction. (**D**) Boxed region of C: arrows indicate side branches from filaments parallel to the edge of the hole. Scale bars: A, 100 nm; A′, 5 μm; A″, 1 μm; B, 50 nm; C, 100 nm; C′, 1 μm; D, 50 nm.

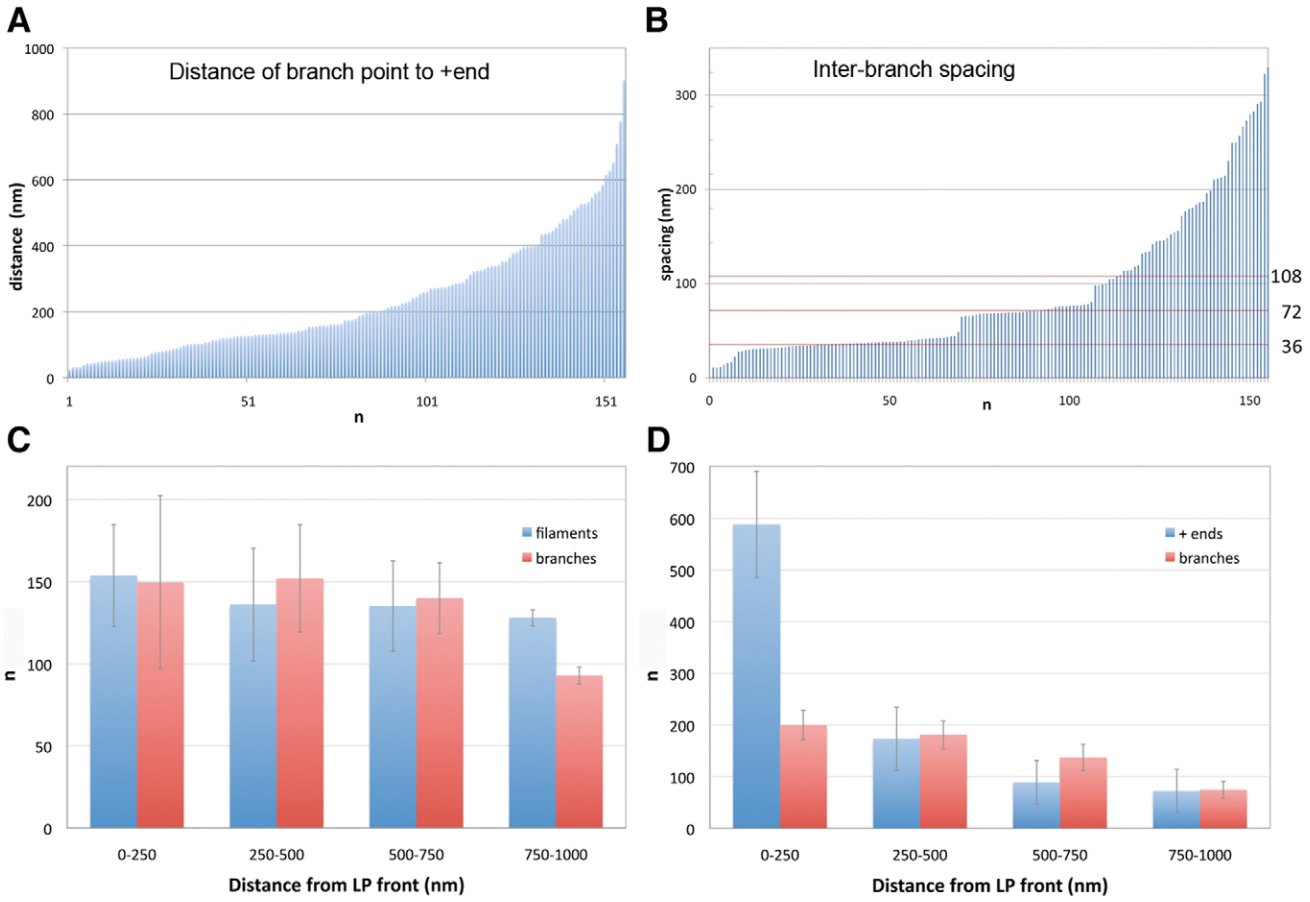

Fig. 6. Quantification of actin branch organization in Rac-induced lamellipodia. (**A**) Distance between branch junctions and filament plus ends, up to 900 nm, which is the limit of the tomograms ($n=155$). (**B**) Spacing between branch junctions along the same filament showing correspondence to multiples of the actin helix repeat (36 nm) for closely spaced events ($n=155$). (**C**) Branch junction and actin filament density distribution through the lamellipodium network. The numbers of branches (total 1140) in lamellipodia (LP) was counted in 0.25 µm wide stripes parallel to and at the indicated distance from the front. Actin filament density is expressed as the number of filament crossing planes through the center of the stripes used for measurements of branch density. Data are from a total of five cells. (**D**) Density of branch junctions across lamellipodia (total 702) compared with the density of filament plus ends (total 957) measured in 250 nm stripes parallel to and at the indicated distance from the front. Data were obtained from four cells.

The induction of a hole in the cytoplasm by a microneedle results in the accumulation of these filaments parallel to the periphery of the hole where they evidently serve as docking platforms for Arp2/3 complexes recruited by WAVE complexes on the plasmalemma. Branching from the sides of these mother filaments constitutes the first step in lamellipodium formation (Fig. 8A,B). A similar process was recently observed in vitro using glass rods coated with the WASP/WAVE C-terminal domain, whereby actin filament primers lying along the rod surface served as platforms for side branching (Achard et al., 2010). The initiation of lamellipodia in this way probably mirrors the initiation of lamellipodia from quiescent regions of the cell periphery, which are delimited by parallel arrays of actin filaments (Small and Celis, 1978). These latter arrays themselves arise through reorganizations of lamellipodia and filopodia associated with the suppression of protrusive activity (Koestler et al., 2008) and cytoskeleton recycling (Nemethova et al., 2008). The daughter filaments that initiate lamellipodia by side branching then serve as the mother filaments for end branching, to continue and maintain lamellipodia protrusion (Fig. 8B,C). From the observed spacing of branch sites the frequency of end branching from a single filament appears highly variable. The frequent occurrence of branching events spaced at 36 and 72 nm was, however, conspicuous. Experiments involving photobleaching of B16 melanoma cells indicate a half-life of the WAVE complex at the lamellipodium tip in the order of 9 seconds (Lai et al., 2008). One WAVE complex could thus initiate many branching events from the same filament if associated, for example, with a complex tracking the filament plus end (Breitsprecher et al., 2011; Dickinson, 2009).

Once a lamellipodium of diagonally arranged filaments has been initiated, the question arises as to why further branching is required to maintain it, because elongation could be supported by proteins such as VASP family members, which localize to the lamellipodium tip (Rottner et al., 1999a). But branching continues during protrusion and treadmilling and each branching event causes an increase in filament number, with the consequence that filaments must be cycled out of the network to maintain a constant filament density. According to the dendritic nucleation model (Pollard and Borisy, 2003) this is achieved by capping filaments rapidly after induction to create a population of short filaments at the front. Our data support the

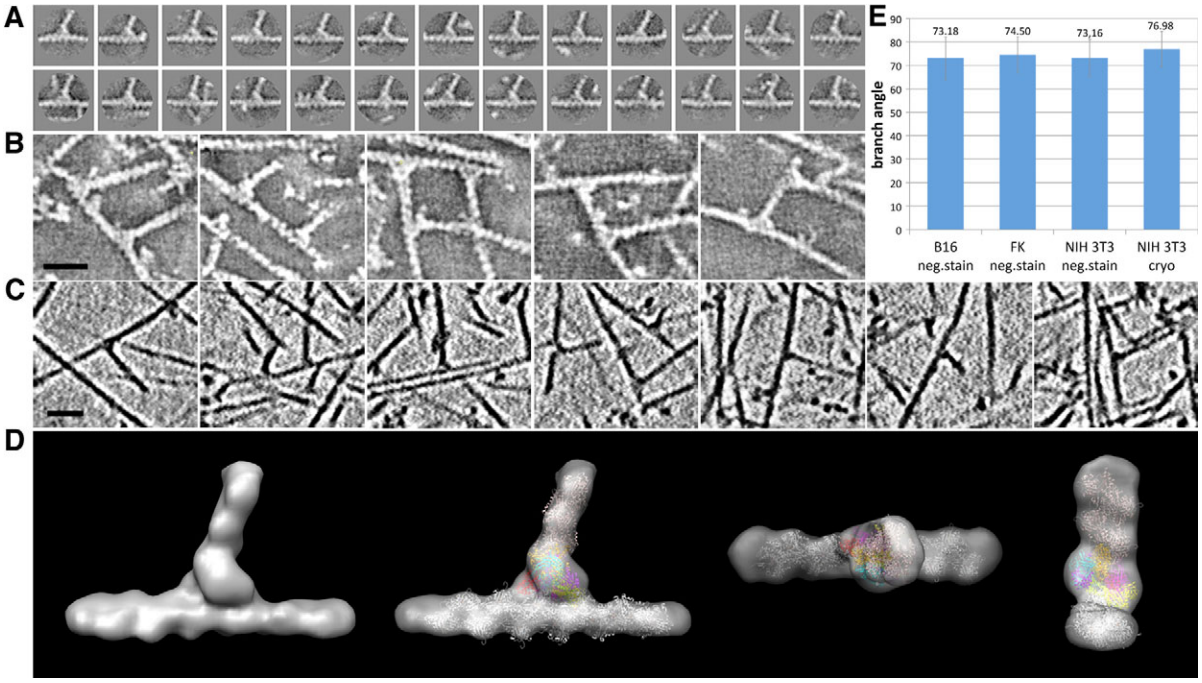

Fig. 7. The in vivo branch junction. (**A**) Gallery of branch junctions selected from tomograms of negatively stained NIH3T3 cell cytoskeletons. (**B**) Examples of multiple branch junctions in close proximity in cells as in A. (**C**) Branch junctions in tomograms of NIH3T3 cell cytoskeletons embedded in vitreous ice. (**D**) Structure obtained from image averaging of branch junctions in negatively stained cytoskeletons, with the molecular model of actin and the Arp2/3 complex superimposed (see also supplementary material Movie 6). The molecular model shows the different parts as follows: mother filament (white), daughter filament (light pink), Arp2 (golden), Arp3 (violet), ArpC1 (turquoise), ArpC2 (yellow), ArpC3 (red), ArpC4 (light green) and ArpC5 (purple). (**E**) Mean values of branch angles measured in cytoskeletons after negative staining or in vitreous ice in the cell types indicated. Scale bars: B,C, 25 nm.

idea that filaments must be regularly capped to balance duplications introduced by branching (Schaub et al., 2007) but not to generate short filaments. We further suggest that capping contributes to molding of the lamellipodium leaflet (Fig. 8A). Mejillano et al. have shown that lamellipodium formation requires capping protein (Mejillano et al., 2004), which localizes towards the tips of lamellipodia (Lai et al., 2008; Mejillano et al., 2004) and treadmills with the actin network over the anterior region of the lamellipodium (Iwasa and Mullins, 2007). Capping protein is therefore strategically located to compete with actin nucleators and elongators in the zone of active polymerization at the tip. Actin branching can in principle occur from any position along the actin helix and as we show branching gives rise to a population of daughter filaments that grow to different degrees out of the horizontal plane of the lamellipodium and terminate on the surface of the actin network. We suppose that there is a narrow zone at the lamellipodium tip in which the concentrations of WAVE and VASP are high enough to compete against capping protein for actin filament plus ends (Fig. 8). However, any filament plus end that falls behind this zone can be capped by capping protein. This would be the probable fate, sooner or later, of actin filaments oriented out of the horizontal plane. Once capped, these filaments could set the initial boundaries of the lamellipodium leaflet. Such a scheme is consistent with the effect of capping protein on the diameter of actin comet tails induced on beads in vitro (Pantaloni et al., 2000). Because the capping zone is apparently narrow (Mejillano et al., 2004; Iwasa and Mullins, 2007; Lai et al., 2008) we assume that filaments ultimately become uncapped (Fig. 8D) but fail to grow because of the local absence of elongation factors. This leaves open the question of what defines the thickness of the lamellipodium in the first place. We speculate that the thickness could be determined by the dimension of the actin bundles at the cell periphery that serve as substrates for lamellipodia initiation (Fig. 8A). As we have shown previously, bundles on the cell edge can derive from filopodia, whose thickness is in the same range as lamellipodia. The curvature of the membrane at the periphery could also be a factor in recruiting the actin nucleation machinery to the plasmalemma (Zhao et al., 2011) and limiting the dimensions of the lamellipodium tip.

Using the observed structural parameters of lamellipodia organization we developed a two-dimensional stochastic simulation model of filament assembly (Fig. 8D; supplementary material Movie 8). The simulation region is close to the leading edge, where we assume the effects of filament disassembly can be neglected. Depolymerization of the network at the rear is not yet considered. This model simulates lamellipodium extension, starting from a pre-established network initiated by filament side branching (as above), in which the angle that filaments subtend to the front is stochastically distributed as in the protruding Rac-induced lamellipodium (supplementary material Fig. S1). The modeling compares with other approaches, where filaments are treated as stiff or flexible rods with stochastic processes describing nucleation, branching, polymerization and capping (Alberts and Odell, 2004; Schaus et al., 2007; Carlsson, 2001; Schreiber et al., 2010). We limited ourselves to a minimal number of factors sufficient to reproduce the essential average properties extracted from tomograms. Filaments are modeled as stiff rods, immobile relative to the substrate. Uncapped barbed ends are tethered (Dickinson, 2009) to a straight leading edge,

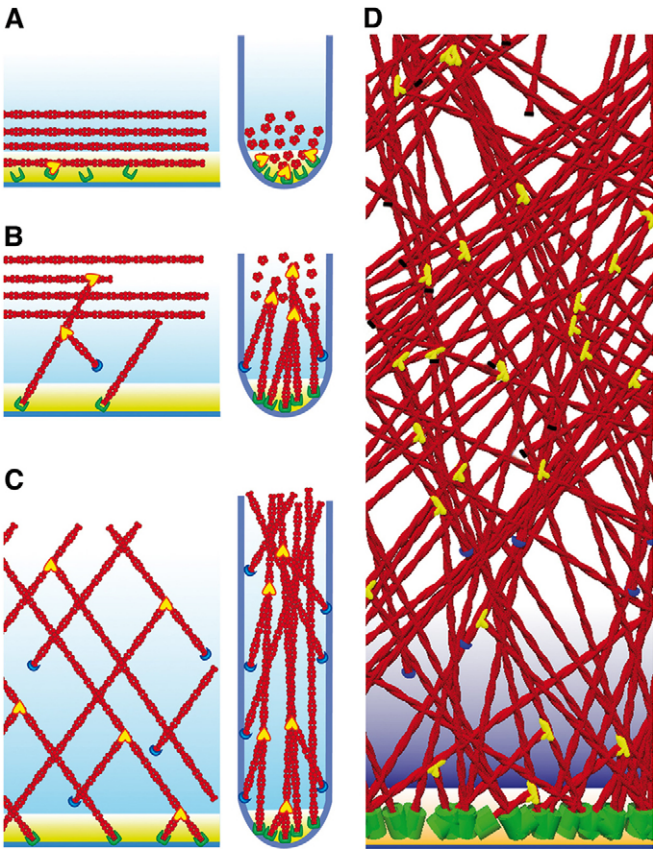

Fig. 8. Proposed scheme of lamellipodium formation and mathematical model of protrusion. (**A**) Plan and cross sectional views of a cell edge primed to form a lamellipodium. Nucleation-promoting and elongation complexes (collectively shown as green brackets), recruited to the membrane (blue line) downstream of signaling events recruit Arp2/3 complexes (yellow hearts) that simultaneously dock onto actin filaments (red) parallel to the cell membrane. (**B**) Lamellipodium initiation occurs by side branching from 'mother filaments' that were parallel to and abutting the plasmalemma. Actin nucleation (by WAVE) and elongation by VASP (and possibly formins) takes place in a narrow zone at the lamellipodium tip (yellow). The plus ends of filaments that branch at angles substantially out of the plane of the lamellipodium trail behind other filaments within the plane, fall out of the yellow polymerization zone and become capped by capping protein (blue crescents). (**C**) Network maintenance involves branching of actin filament ends at the plasmalemma and gives rise to a continuum of distances between branch junctions and the lamellipodium tip. Capping protein continues to terminate the growth of filaments branching out of the plane of the lamellipodium, and the ends of these filaments set the dorsal and ventral boundaries of the network. (**D**) A single movie frame of the mathematical simulation of protrusion. Filaments tipped with black were formerly capped, but become uncapped as they move out of the capping zone close to the front (Discussion; supplementary material Movie 8). Other symbols as in A–C.

resulting in an angle-dependent polymerization rate (Mogilner and Oster, 1996). The protrusion speed is set to v_{prot}= 2 μm/minute, as observed for the protruding Rac-induced lamellipodium. The simulation domain is a rectangular region. Lateral inward flow of filaments through the sides is prescribed at a rate reproducing the number of inward pointing filaments in the corresponding region of the tomogram (Fig. 1F,G). This typically leads to different rates of inward and outward lateral flow, in contrast to the scheme of Schaus et al. where cyclic lateral boundary conditions were used (Schaus et al., 2007). Branching and capping of filaments are assumed to occur directly at the leading edge (with capping taking place just behind the polymerization zone at the tip) where the branching rate, k_{br}=0.042/second (per filament) and capping rate, k_{cap}=0.03/second are chosen such that the long time average of the total number of branch points generated (98) and the total filament length (60.3 μm) in the simulation domain of the movie (area 0.49 μm^2) match the corresponding numbers identified in the tomogram. The average distance between branching points can be computed as 0.61 μm.

Where more or less symmetrical diagonal meshworks of actin filaments are observed, it seems most likely that actin branching plays a main role in setting them up. Lamellipodia are not, however, homogeneous in their organization and intermediate assemblies can play a role in modulating protrusion rate (Koestler et al., 2008) and in transitions from lamellipodia to filopodia (Small, 1981; Svitkina et al., 2003; Urban et al., 2010), probably involving VASP family proteins and formins (Faix and Rottner, 2006; Mattila and Lappalainen, 2008). To gain further insight into the nature of these transitions, electron tomography will be an essential complement to determine the structural changes associated with experimental manipulations of the actin nanomachinery.

Materials and Methods

Cell culture, transfection and fixation

B16 melanoma cells were cultivated as previously described (Koestler et al., 2008) and transfected with Fugene HD (Roche), according to the manufacturer's instructions. Cells were transfected with mCherry–actin (Nemethova et al., 2008), EGFP–Arp-p16 [ArpC5 (Lai et al., 2008)], mCherry–VASP (Koestler et al., 2008), GFP–Abi-1 (Lai et al., 2008) and EGFP–myosin-light-chain (Nemethova et al., 2008). NIH3T3 cells were cultured in high glucose DMEM with 10% fetal bovine serum (FBS; Sigma), 2 mM L-glutamine, 1 mM sodium pyruvate and 1% penicillin and streptomycin at 37℃ in the presence of 5% CO_2. Cells were transfected using Lipofectamine LTX (Invitrogen): the primary transfection mix (200 μl Optimem, 2 μg DNA, 2 μg Lipofectamine Plus) was incubated for 10 minutes, then 5 μl Lipofectamine LTX was added and the mixture incubated for a further 30 minutes. The cells were plated for 5 hours in six-well plates and then incubated with the transfection mix overnight. The plasmids employed were: pEGFP-actin (Clontech), EGFP-LifeAct (Riedl et al., 2008) and myc-L61Rac (kindly provided by Laura Machesky, Beatson Institute, Glasgow, UK).

For live cell microscopy, cells were plated onto glass coverslips carrying a Formvar film (see below) coated with 25 μg/ml laminin (Sigma) in laminin coating buffer (150 mM NaCl, 50 mM Tris, pH 7.5) for B16 cells or 50 μg/ml fibronectin (Sigma) in PBS for NIH3T3 cells. Fish keratocytes were prepared from freshly killed brook trout (*Salvelinus fontinalis*) as previously described (Urban et al., 2010). NIH3T3 and B16 cells were simultaneously extracted and fixed with 0.5% Triton X-100 (Fluka) and 0.25% glutaraldehyde (Agar Scientific, Stansted, UK) in cytoskeleton buffer (10 mM MES buffer, 150 mM NaCl, 5 mM EGTA, 5 mM glucose and 5 mM $MgCl_2$, at pH 6.1), and keratocytes in a mixture of 0.75% Triton X-100 and 0.25% glutaraldehyde in cytoskeleton buffer pH 6.8. An initial fixation of 1 minute in this mixture was followed by post-fixation for 15 minutes in cytoskeleton buffer (pH 7) containing 2% glutaraldehyde and 1 μg/ml phalloidin, to stabilize the actin filaments. The coverslips were then stored in cytoskeleton buffer containing 2% glutaraldehyde with 10 μg/ml phalloidin at 4℃, before processing for electron microscopy. Negative staining was performed in mixtures of 4–6% sodium silicotungstate (Agar Scientific) at pH 7, containing 10 nm gold colloid saturated with bovine serum albumin (BSA) diluted 1:10 from a gold stock (Urban et al., 2010).

Correlated live cell imaging for electron tomography

In order to analyze the ultrastructure of lamellipodia whose history of protrusive activity is known, cells were grown on Formvar-coated coverslips and first imaged live and fixed on the fluorescence microscope. In the electron microscope, relocation of the same cells was facilitated by embossing the Formvar films when on the coverslips with a finder grid pattern in gold (Auinger and Small, 2008). Light microscopy was performed at 37℃ (NIH3T3 and B16F1 cells) or room temperature (fish keratocytes) on an inverted Zeiss Axioscope equipped with epifluorescence optics using a 100× phase-contrast lens, and a halogen lamp as a light source (Zeiss). Time-lapse images were recorded on a Roper Micromax, 512×512 rear-illuminated, cooled CCD camera controlled by Metamorph software

at intervals of 2–10 seconds. Following imaging with the light microscope and fixation on the microscope stage, the Formvar film was peeled from the coverslip under buffer, inverted, and floated on the buffer surface cell-side down. The central square of an electron microscope grid (100 mesh copper–palladium) was positioned over the region occupied by the filmed cells using a micromanipulator under a dissecting microscope (Auinger and Small, 2008). The film and grid were recovered with a piece of Parafilm, and the cells were rinsed and dried in negative stain containing the gold colloid.

Cell microinjection and manipulation

Microinjection and micromanipulation were performed using Eppendorf (Hamburg, Germany) microinjection needles mounted on a Leitz (Vienna, Austria) micromanipulator with 100× phase-contrast optics. Backpressure and injection pulses were generated using an Eppendorf Femtojet. Recombinant L61 Rac for microinjection (a kind gift from Jan Faix, Hannover Medical School, Germany) was purified as described previously (Rottner et al., 1999b) and used at a concentration of 1 mg/ml in microinjection buffer (150 mM Tris pH 7.5, 150 mM NaCl, 5 mM $MgCl_2$, 1 mM dithiothreitol). To generate wounds in the cytoplasm, an unfilled needle tip was lowered gently onto the cell and removed immediately after the hole was induced, to avoid damage to the underlying Formvar film. Several holes could be induced in the same cell and then fixed at different stages of repair.

Cryo-electron tomography

For cryo-electron microscopy, L61Rac-transfected NIH3T3 cells were plated in growth medium onto Quantifoil R1/4 (Jena) perforated carbon film on 200-mesh gold grids, and allowed to spread overnight. Cytoskeletons were prepared by fixation in a glutaraldehyde–Triton mixture as described above. Blotting and freezing of grids was performed using a grid-plunging device (EMGP, Leica Microsystems, Vienna, Austria) that allows blotting in a controlled humidity on the back of the grid to avoid any contact with the cells (Resch et al., 2011).

Electron tomography

Tilt series of negatively stained cytoskeletons on Formvar-coated copper–palladium grids (Maxtaform), and vitreously frozen cytoskeletons on Quantifoil R1/4 perforated carbon film on 200-mesh gold grids, were acquired on a FEI Tecnai F30 (Polara) microscope, operated at 300 kV and cooled to approximately 80 K for both types of specimen. Automated acquisition of tilt series was driven by SerialEM versions 2.7.x and 2.8.x. Typically, the tilt range was −60 to +60 using the Saxton tilt scheme based on 1° increments (negative stain) and 2° increments (frozen, hydrated samples) at a defocus value of –3 µm and –10 µm for the negatively stained and frozen samples, respectively. For the negatively stained samples, tomograms were generated from two tilt series obtained around orthogonal axes and images were recorded on a Gatan UltraScan 4000 CCD camera. The primary on-screen magnifications used for image acquisition were 27,500× for the negatively stained samples and 20,500× for the cryofixation samples.

The total electron dose for the frozen, hydrated samples was maximally 80–150 electrons/$Å^2$ in regions of free ice over holes in the support film.

Filament tracking, quantification and orientation analysis

Re-projections from the tilt series were generated using IMOD software from the Boulder Laboratory for 3D Electron Microscopy of Cells, University of Colorado Boulder, CO (Mastronarde, 2005), using the gold particles as fiducials for alignments and the simultaneous iterative reconstruction technique (SIRT) algorithm for re-projections of the cryo data. Filaments were tracked manually using IMOD, essentially as described previously (Urban et al., 2010), or automatically using custom developed software (Winkler et al., 2012). Correlation of manual and automatic tracking data was performed to avoid assignment of contaminating background debris to actin filaments. Filament orientation was analyzed by computing the length and horizontal angle between consecutive points along filaments and summing up the lengths of segments within the same angle range. Angles between filaments at branch junctions were computed from three coordinates in the tomogram, one at the branch point and one on each intersecting filament 30–50 nm from the branch point. For filament counts, vertical planes were generated in the tomograms at different distances from the lamellipodium front and all filaments that crossed the planes were marked and scored (Urban et al., 2010). For measurements of the density of branch junctions and filament plus ends, lamellipodia were divided into 0.25 µm wide stripes parallel to the cell front and the number of identified branches and plus ends counted in the projected tomogram model.

Image analysis of branch junctions

For structural analysis of branch junctions, NIH3T3 cells transfected with Rac were plated onto either fibronectin-coated Formvar films (as above) or on polylysine-coated Quantifoil films (R1/4) containing 1 µm holes that were additionally covered with a thin carbon film and fixed and stained as above. To promote spreading on the Quantifoil films, cells were maintained in serum-free medium for 4–5 hours after settling on the grids for 1–2 hours. The junctions in the tomograms were marked by hand using IMOD, and subtomograms (48 nm^3) around the marked points were extracted. A simple branched cylinder was generated on computer as the initial reference. The subtomograms were three-dimensionally aligned to the reference and averaged. The averaged structure was used for the next reference and the whole procedure was iterated until the averaged structure was converged.

Fitting atomic structures into the branch model

The actin filament model [2ZWH (Oda et al., 2009)] containing respectively 12 and 5 subunits were fitted into the mother filament and the daughter filament in the averaged branch structure. The density attributed to the two filaments was subtracted from the map. The Arp2 and ARPC3 were removed from the Arp2/3 crystal structure [2P9I (Nolen and Pollard, 2007)] and the other components, Arp3, ARPC1, ARPC2, ARPC4 and ARPC5 were fitted into the remaining mass of the branch as a rigid body, without changing relative position and orientation of each component in the crystal. The density due to the fitted components of the Arp2/3 complex was removed from the map again. The two components, Arp2 and ARPC3, were excluded from the rigid body fitting because they did not fit well. An Arp2 model was constructed by replacing half of the Arp2, which was disordered in the crystal, by the corresponding part of the actin subunit in the filament (2ZWH). The Arp2 model and the crystal structure of ARPC3 in 2P9I were fitted to the remaining density of the branch independently. The fitting was performed using Chimera software (Pettersen et al., 2004) and the other calculations were performed using EOS software (Yasunaga and Wakabayashi, 1996).

Image analysis of filament polarity

The traces of the filaments were interpolated by a three-dimensional spline curve and subtomograms including the actin filaments were extracted along the spline curves. The actin filament in the extracted subtomogram was traced again automatically by correlation with a three-dimensional cylinder. The filament was unbent according to the trace. The unbent filament was two-dimensionally projected onto a plane including the filament axis with the smallest tilt angle against the grid plane. The projected images were analyzed using the single particle analysis procedures for filamentous complexes (Narita and Maéda, 2007) and the filament polarity was determined. The details of the analysis will be described elsewhere (Narita et al., 2012).

Stochastic simulation of actin assembly

The mathematical simulation was performed on a growing two-dimensional rectangular region, representing a section of the lamellipodium, bounded on one side by a segment of the leading edge, which moves with a constant prescribed protrusion speed. The simulation is started with a randomly chosen, un-branched network of straight filaments with an angular distribution as determined from a typical tomogram (supplementary material Fig. S1E,F). Initially, all barbed ends are attached to the leading edge, and all pointed ends are outside the simulation domain. The filaments remain straight and immobile relative to the substrate. Their dynamics is the result of polymerization, branching, capping and lateral flow, including inflow of filaments through the sides of the simulation domain. The polymerization rate of individual filaments is angle dependent such that the barbed ends stay attached to the leading edge. Branching and capping are described as stochastic processes, whose rates influence network geometry and are used as fitting parameters. Branching events happen with a fixed branching angle and are only accepted, if the new filament is directed towards the leading edge. For practical purposes of the simulation, capping occurs at the front edge, but is assumed to occur slightly behind the front, outside the polymerization zone (see text). Capping stops polymerization and leads to a barbed end falling behind the leading edge. Uncapping is also described as a stochastic processes, but without any effect on the filament dynamics because uncapped filaments with barbed ends away from the leading edge do not resume polymerization, reflecting the assumption that polymerization is driven by an agent only available at the leading edge. Finally, the rate of filaments entering the simulation domain through the sides and their angular distribution are chosen stochastically, to reproduce the actual filament organization observed in the tomograms.

Acknowledgements

We thank Tibor Kulcsar for assistance with graphics.

Funding

This work was supported by the Austrian Science Fund [projects FWF I516-B09 and FWF P21292-B09 to J.V.S.]; the Vienna Science and Technology Fund [WWTF- grant numbers MA 09-004 to J.V.S. and C.S], ZIT - The Technology Agency of the City of Vienna [VSOE, CMCN to J.V.S. and G.P.R.]; the Deutsche Forschungsgemeinschaft [grant number RO 2414/1-2 to K.R.]; the Daiko research foundation [grant number 9134 to A.N.]; and a Grant-in-Aid for Scientific

Research [S, grant number 20227008 to Y.M.] and a Grant-in-Aid for Young Scientists [B, grant number 22770145 to A.N.] (B) from The Ministry of Education, Culture, Sports, Science and Technology of the Japanese Government. Deposited in PMC for immediate release.

Supplementary material available online at
http://jcs.biologists.org/lookup/suppl/doi:10.1242/jcs.107623/-/DC1

References

Abercrombie, M., Heaysman, J. E. and Pegrum, S. M. (1970). The locomotion of fibroblasts in culture. I. Movements of the leading edge. *Exp. Cell Res.* **59**, 393-398.

Abercrombie, M., Heaysman, J. E. and Pegrum, S. M. (1971). The locomotion of fibroblasts in culture: IV. Electron microscopy of the leading lamella. *Exp. Cell Res.* **67**, 359-367.

Achard, V., Martiel, J.-L., Michelot, A., Guérin, C., Reymann, A.-C., Blanchoin, L. and Boujemaa-Paterski, R. (2010). A "primer"-based mechanism underlies branched actin filament network formation and motility. *Curr. Biol.* **20**, 423-428.

Alberts, J. B. and Odell, G. M. (2004). In silico reconstitution of Listeria propulsion exhibits nano-saltation. *PLoS Biol.* **2**, e412.

Alexandrova, A. Y., Arnold, K., Schaub, S., Vasiliev, J. M., Meister, J. J., Bershadsky, A. D. and Verkhovsky, A. B. (2008). Comparative dynamics of retrograde actin flow and focal adhesions: formation of nascent adhesions triggers transition from fast to slow flow. *PLoS ONE* **3**, e3234.

Amann, K. J. and Pollard, T. D. (2001). The Arp2/3 complex nucleates actin filament branches from the sides of pre-existing filaments. *Nat. Cell Biol.* **3**, 306-310.

Auinger, S. and Small, J. V. (2008). Correlated light and electron microscopy of the cytoskeleton. *Methods Cell Biol.* **88**, 257-272.

Breitsprecher, D., Kiesewetter, A. K., Linkner, J., Vinzenz, M., Stradal, T. E., Small, J. V., Curth, U., Dickinson, R. B. and Faix, J. (2011). Molecular mechanism of Ena/VASP-mediated actin-filament elongation. *EMBO J.* **30**, 456-467.

Campellone, K. G. and Welch, M. D. (2010). A nucleator arms race: cellular control of actin assembly. *Nat. Rev. Mol. Cell Biol.* **11**, 237-251.

Carlsson, A. E. (2001). Growth of branched actin networks against obstacles. *Biophys. J.* **81**, 1907-1923.

Chesarone, M. A. and Goode, B. L. (2009). Actin nucleation and elongation factors: mechanisms and interplay. *Curr. Opin. Cell Biol.* **21**, 28-37.

Dickinson, R. B. (2009). Models for actin polymerization motors. *J. Math. Biol.* **58**, 81-103.

Faix, J. and Rottner, K. (2006). The making of filopodia. *Curr. Opin. Cell Biol.* **18**, 18-25.

Flanagan, L. A., Chou, J., Falet, H., Neujahr, R., Hartwig, J. H. and Stossel, T. P. (2001). Filamin A, the Arp2/3 complex, and the morphology and function of cortical actin filaments in human melanoma cells. *J. Cell Biol.* **155**, 511-517.

Henson, J. H., Nazarian, R., Schulberg, K. L., Trabosh, V. A., Kolnik, S. E., Burns, A. R. and McPartland, K. J. (2002). Wound closure in the lamellipodia of single cells: mediation by actin polymerization in the absence of an actomyosin purse string. *Mol. Biol. Cell* **13**, 1001-1014.

Höglund, A.-S., Karlsson, R., Arro, E., Fredriksson, B.-A. and Lindberg, U. (1980). Visualization of the peripheral weave of microfilaments in glia cells. *J. Muscle Res. Cell Motil.* **1**, 127-146.

Insall, R. H. (2011). Dogma bites back - the evidence for branched actin. *Trends Cell Biol.* **21**, 4-5.

Iwasa, J. H. and Mullins, R. D. (2007). Spatial and temporal relationships between actin-filament nucleation, capping, and disassembly. *Curr. Biol.* **17**, 395-406.

Koestler, S. A., Auinger, S., Vinzenz, M., Rottner, K. and Small, J. V. (2008). Differentially oriented populations of actin filaments generated in lamellipodia collaborate in pushing and pausing at the cell front. *Nat. Cell Biol.* **10**, 306-313.

Lai, F. P., Szczodrak, M., Block, J., Faix, J., Breitsprecher, D., Mannherz, H. G., Stradal, T. E., Dunn, G. A., Small, J. V. and Rottner, K. (2008). Arp2/3 complex interactions and actin network turnover in lamellipodia. *EMBO J.* **27**, 982-992.

Lämmermann, T. and Sixt, M. (2009). Mechanical modes of 'amoeboid' cell migration. *Curr. Opin. Cell Biol.* **21**, 636-644.

Machesky, L. M. and Insall, R. H. (1998). Scar1 and the related Wiskott-Aldrich syndrome protein, WASP, regulate the actin cytoskeleton through the Arp2/3 complex. *Curr. Biol.* **8**, 1347-1356.

Mastronarde, D. N. (2005). Automated electron microscope tomography using robust prediction of specimen movements. *J. Struct. Biol.* **152**, 36-51.

Mattila, P. K. and Lappalainen, P. (2008). Filopodia: molecular architecture and cellular functions. *Nat. Rev. Mol. Cell Biol.* **9**, 446-454.

Mejillano, M. R., Kojima, S., Applewhite, D. A., Gertler, F. B., Svitkina, T. M. and Borisy, G. G. (2004). Lamellipodial versus filopodial mode of the actin nanomachinery: pivotal role of the filament barbed end. *Cell* **118**, 363-373.

Mitchison, T. and Kirschner, M. (1988). Cytoskeletal dynamics and nerve growth. *Neuron* **1**, 761-772.

Mogilner, A. and Oster, G. (1996). Cell motility driven by actin polymerization. *Biophys. J.* **71**, 3030-3045.

Narita, A. and Maeda, Y. (2007). Molecular determination by electron microscopy of the actin filament end structure. *J. Mol. Biol.* **365**, 480-501.

Narita, A., Mueller, J., Urban, E, Vinzenz, M., Small, J. V. and Maeda, Y. (2012). Direct determination of actin polarity in the cell. *J. Mol. Biol.* **419**, 359-368.

Nemethova, M., Auinger, S. and Small, J. V. (2008). Building the actin cytoskeleton: filopodia contribute to the construction of contractile bundles in the lamella. *J. Cell Biol.* **180**, 1233-1244.

Nolen, B. J. and Pollard, T. D. (2007). Insights into the influence of nucleotides on actin family proteins from seven structures of Arp2/3 complex. *Mol. Cell* **26**, 449-457.

Oda, T., Iwasa, M., Aihara, T., Maéda, Y. and Narita, A. (2009). The nature of the globular- to fibrous-actin transition. *Nature* **457**, 441-445.

Pantaloni, D., Boujemaa, R., Didry, D., Gounon, P. and Carlier, M.-F. (2000). The Arp2/3 complex branches filament barbed ends: functional antagonism with capping proteins. *Nat. Cell Biol.* **2**, 385-391.

Pettersen, E. F., Goddard, T. D., Huang, C. C., Couch, G. S., Greenblatt, D. M., Meng, E. C. and Ferrin, T. E. (2004). UCSF Chimera--a visualization system for exploratory research and analysis. *J. Comput. Chem.* **25**, 1605-1612.

Pollard, T. D. and Borisy, G. G. (2003). Cellular motility driven by assembly and disassembly of actin filaments. *Cell* **112**, 453-465.

Pollard, T. D. and Cooper, J. A. (2009). Actin, a central player in cell shape and movement. *Science* **326**, 1208-1212.

Resch, G. P., Brandstetter, M., Pickl-Herk, A. M., Königsmaier, L., Wonesch, V. I. and Urban, E. (2011). Immersion freezing of biological specimens: rationale, principles, and instrumentation. *Cold Spring Harb. Protoc.* **2011**, 778-782.

Riedl, J., Crevenna, A. H., Kessenbrock, K., Yu, J. H., Neukirchen, D., Bista, M., Bradke, F., Jenne, D., Holak, T. A., Werb, Z. et al. (2008). Lifeact: a versatile marker to visualize F-actin. *Nat. Methods* **5**, 605-607.

Rottner, K. and Stradal, T. E. B. (2011). Actin dynamics and turnover in cell motility. *Curr. Opin. Cell Biol.* **23**, 569-578.

Rottner, K., Behrendt, B., Small, J. V. and Wehland, J. (1999a). VASP dynamics during lamellipodia protrusion. *Nat. Cell Biol.* **1**, 321-322.

Rottner, K., Hall, A. and Small, J. V. (1999b). Interplay between Rac and Rho in the control of substrate contact dynamics. *Curr. Biol.* **9**, 640-648.

Rouiller, I., Xu, X. P., Amann, K. J., Egile, C., Nickell, S., Nicastro, D., Li, R., Pollard, T. D., Volkmann, N. and Hanein, D. (2008). The structural basis of actin filament branching by the Arp2/3 complex. *J. Cell Biol.* **180**, 887-895.

Schaub, S., Meister, J. J. and Verkhovsky, A. B. (2007). Analysis of actin filament network organization in lamellipodia by comparing experimental and simulated images. *J. Cell Sci.* **120**, 1491-1500.

Schaus, T. E., Taylor, E. W. and Borisy, G. G. (2007). Self-organization of actin filament orientation in the dendritic-nucleation/array-treadmilling model. *Proc. Natl. Acad. Sci. USA* **104**, 7086-7091.

Schreiber, C. H., Stewart, M. and Duke, T. (2010). Simulation of cell motility that reproduces the force-velocity relationship. *Proc. Natl. Acad. Sci. USA* **107**, 9141-9146.

Small, J. V. (1981). Organization of actin in the leading edge of cultured cells: influence of osmium tetroxide and dehydration on the ultrastructure of actin meshworks. *J. Cell Biol.* **91**, 695-705.

Small, J. V. and Celis, J. E. (1978). Filament arrangements in negatively stained cultured cells: the organization of actin. *Cytobiologie* **16**, 308-325.

Small, J. V., Isenberg, G. and Celis, J. E. (1978). Polarity of actin at the leading edge of cultured cells. *Nature* **272**, 638-639.

Small, J. V., Stradal, T., Vignal, E. and Rottner, K. (2002). The lamellipodium: where motility begins. *Trends Cell Biol.* **12**, 112-120.

Small, J. V., Winkler, C., Vinzenz, M. and Schmeiser, C. (2011). Reply: Visualizing branched actin filaments in lamellipodia by electron tomography. *Nat. Cell Biol.* **13**, 1013-1014.

Steinmetz, M. O., Stoffler, D., Hoenger, A., Bremer, A. and Aebi, U. (1997). Actin: from cell biology to atomic detail. *J. Struct. Biol.* **119**, 295-320.

Svitkina, T. M. and Borisy, G. G. (1999). Arp2/3 complex and actin depolymerizing factor/cofilin in dendritic organization and treadmilling of actin filament array in lamellipodia. *J. Cell Biol.* **145**, 1009-1026.

Svitkina, T. M., Verkhovsky, A. B., McQuade, K. M. and Borisy, G. G. (1997). Analysis of the actin-myosin II system in fish epidermal keratocytes: mechanism of cell body translocation. *J. Cell Biol.* **139**, 397-415.

Svitkina, T. M., Bulanova, E. A., Chaga, O. Y., Vignjevic, D. M., Kojima, S., Vasiliev, J. M. and Borisy, G. G. (2003). Mechanism of filopodia initiation by reorganization of a dendritic network. *J. Cell Biol.* **160**, 409-421.

Urban, E., Jacob, S., Nemethova, M., Resch, G. P. and Small, J. V. (2010). Electron tomography reveals unbranched networks of actin filaments in lamellipodia. *Nat. Cell Biol.* **12**, 429-435.

Wang, Y. L. (1985). Exchange of actin subunits at the leading edge of living fibroblasts: possible role of treadmilling. *J. Cell Biol.* **101**, 597-602.

Waterman-Storer, C. M., Desai, A., Bulinski, J. C. and Salmon, E. D. (1998). Fluorescent speckle microscopy, a method to visualize the dynamics of protein assemblies in living cells. *Curr. Biol.* **8**, 1227-1230.

Welch, M. D., DePace, A. H., Verma, S., Iwamatsu, A. and Mitchison, T. J. (1997). The human Arp2/3 complex is composed of evolutionarily conserved subunits and is localized to cellular regions of dynamic actin filament assembly. *J. Cell Biol.* **138**, 375-384.

Winkler, C., Vinzenz, M., Small, J. V. and Schmeiser, C. (2012). Actin filament tracking by the localized Radon transform in three-dimensional electron microscope tomograms of lamellipodia. *J. Struct. Biol.* **178**, 19-28.

Yang, C. and Svitkina, T. (2011). Visualizing branched actin filaments in lamellipodia by electron tomography. *Nat. Cell Biol.* **13**, 1012-1013.

Yasunaga, T. and Wakabayashi, T. (1996). Extensible and object-oriented system Eos supplies a new environment for image analysis of electron micrographs of macromolecules. *J. Struct. Biol.* **116**, 155-160.

Zhao, H., Pykäläinen, A. and Lappalainen, P. (2011). I-BAR domain proteins: linking actin and plasma membrane dynamics. *Curr. Opin. Cell Biol.* **23**, 14-21.

Journal of Cell Science